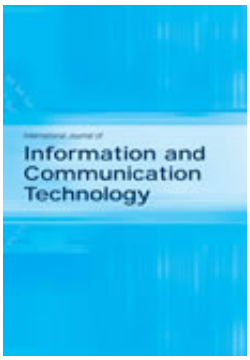

International Journal of Information and Communication Technology

ISSN online: 1741-8070 - ISSN print: 1466-6642
https://www.inderscience.com/ijict

Development of an AI-powered classification model for monitoring construction disturbances using remote sensing data

Jing Yan, Yin Liu, Shengcheng Xie, Yimin An, Yifan Liang

DOI: 10.1504/IJICT.2025.10073710

Article History:

Received:	17 June 2025
Last revised:	28 August 2025
Accepted:	01 September 2025
Published online:	16 October 2025

Development of an AI-powered classification model for monitoring construction disturbances using remote sensing data

Jing Yan*

Marketing Service Center,
State Grid Xinjiang Electric Power Co., Ltd.,
Urumqi, 830000, Xinjiang, China
Email: 15311821827@163.com
*Corresponding author

Yin Liu, Shengcheng Xie, Yimin An and Yifan Liang

Electric Power Research Institute,
State Grid Xinjiang Electric Power Co., Ltd.,
Urumqi, 830000, Xinjiang, China
Email: 253425618@qq.com
Email: 1547573135@qq.com
Email: anyimin01@163.com
Email: 445655517@qq.com

Abstract: In complex settings, the identification and dynamic monitoring of construction disturbance areas still face problems such as insufficient feature extraction, limited generalisation, and unstable multi-temporal detection accuracy. This study proposed a novel multi-level integrated approach that combines fractal network evolution algorithm (FNEA) segmentation, genetic algorithm (GA) global optimisation, and convolutional neural network (CNN) multi-scale feature learning to achieve high-precision disturbance recognition and dynamic monitoring. Experimental results showed that the method achieved an overall accuracy of 95.2% ± 0.4% (95% CI [95.0, 95.4]), maintained an accuracy above 99% in multi-temporal tests, reduced the false alarms and missed detections by 0.7–5.2% compared with baseline methods, and converged within 30 iterations. Compared with existing techniques, the framework provides an intelligent and efficient solution through the joint use of image segmentation, evolutionary optimisation, and deep feature learning, opens a new direction for remote sensing monitoring in complex construction environments.

Keywords: construction disturbance detection; fractal network evolution; genetic algorithm; convolutional neural network; CNN; multi-feature fusion.

Reference to this paper should be made as follows: Yan, J., Liu, Y., Xie, S., An, Y. and Liang, Y. (2025) 'Development of an AI-powered classification model for monitoring construction disturbances using remote sensing data', *Int. J. Information and Communication Technology*, Vol. 26, No. 37, pp.41–58.

Biographical notes: Jing Yan received his Bachelor's degree in Engineering from Northeastern University, China and Master's degree in Engineering from Wuhan University. Currently, he works at Marketing Service Center, State Grid Xinjiang Electric Power Co., Ltd. His research interests include environmental protection and soil and water conservation management in power grid engineering.

Yin Liu received her Bachelor's degree from Changsha University of Science and Technology, China. Currently, she works at Electric Power Research Institute, State Grid Xinjiang Electric Power Co., Ltd. Her research interests include electric power environmental analysis technology.

Shengcheng Xie received his Bachelor's degree from North China Electric Power University, China. Currently, he works at Electric Power Research Institute, State Grid Xinjiang Electric Power Co., Ltd. His research interests include environmental protection and soil and water conservation technology in power grid engineering.

Yimin An received his bachelor's degree from Xi'an Jiaotong University, China. Currently, he works at Electric Power Research Institute, State Grid Xinjiang Electric Power Co., Ltd. His research interests include optimisation and improvement of remote sensing data in power grid engineering.

Yifan Liang received her bachelor's degree from North China Electric Power University, China. Currently, she works at Electric Power Research Institute, State Grid Xinjiang Electric Power Co., Ltd. Her research interests include power grid engineering data analysis and environmental water conservation technology applications.

1 Introduction

Human activities such as urban expansion, infrastructure construction, and mining can lead to significant environmental changes. These anthropogenic impacts may cause vegetation destruction, soil erosion, and alterations in surface thermal conditions, thereby disrupting ecological balance and affecting sustainable environmental development (Lv et al., 2023; Guo et al., 2023). Effective detection of human activities is crucial for environmental management, urban planning, and disaster warning (Darem et al., 2023). However, construction areas exhibit uneven spatial distribution and complex patterns, which challenge traditional methods and often lead to low accuracy and instability. Remote sensing offers large-scale coverage, long multi-temporal, and high spatiotemporal resolution. These advantages provide new opportunities for construction-disturbance monitoring (Liu et al., 2023). When remote sensing data are combined with artificial intelligence techniques, the quality and efficiency of large-scale dataset processing can be significantly improved, enhancing the classification accuracy and adaptability of disturbance detection methods (Padhy et al., 2023). However, machine learning methods based on traditional spectral indices still suffer from high misclassification rates when dealing with complex construction environments. This limitation has driven the development of intelligent detection models, with research focusing on the integration of multi-feature, multi-temporal, and multi-source data.

In studies on construction disturbance area classification, Xu et al. (2022). recommended a classification approach using NDVI and NDBI for separating construction areas from natural surfaces. Experimental results showed that the method achieved 83.5% classification accuracy in typical bare soil regions. However, it was highly sensitive to variations in illumination conditions and soil moisture, leading to a high misclassification rate. Li et al. (2022) further integrated multi-band spectral features and applied a support vector machine (SVM) for classification. Compared to single-index classification methods, the overall accuracy improved by 10%. However, SVM requires manual selection of features and parameter optimisation, limiting its adaptability to different construction areas. To overcome the limitations of traditional machine learning approaches, Zeng et al. (2022) introduced a U-Net deep learning model that automatically extracts high-dimensional features of construction disturbance areas using an end-to-end framework. Their model achieved 92% overall classification accuracy on GF-2 high-resolution imagery. Despite its strong feature extraction capability, U-Net heavily depends on labelled data, restricting its large-scale applicability. Casagli et al. (2023) applied object-based classification by improving segmentation methods, achieving classification stability with an accuracy of over 85% under different terrain conditions. However, the method is highly sensitive to segmentation scale, making automation difficult. Addressing this issue, Wang et al. (2022) introduced a genetic algorithm (GA) to optimise classifier parameters and improve model adaptability. Their results demonstrated a 6.4% increase in classification accuracy over the RF method. However, GA still suffers from local optima in high-dimensional data optimisation and lacks effective temporal information integration for dynamic classification.

For detecting dynamic changes in construction disturbance, Ahmad et al. (2023a) proposed a method based on spectral brightness values, detecting construction activity by calculating pixel values across multiple multi-temporal images. However, their method is sensitive to illumination variations and cloud cover, leading to a high false detection rate. Yang et al. (2023) developed a multi-temporal analysis method that monitors vegetation disturbance trends using NDVI changes. Their study on the Sentinel-2 dataset showed an 85.7% detection accuracy for large-scale construction projects, but its ability to identify bare soil and building zone changes was limited, reducing its applicability. Ahmad et al. (2023b) developed a grey-level co-occurrence matrix (GLCM) texture variation detection method, which effectively captured surface structural changes, achieving a 12.3% improvement in recognition accuracy over traditional spectral analysis methods. However, its high computational complexity poses challenges in processing large-scale construction areas. Shen et al. (2022) introduced shape parameters, such as area and compactness, to construct a temporal detection model. Although it achieved 88.2% accuracy for large-scale construction projects (area > 1 km^2), it exhibited significant omission errors in small disturbance areas (area < 100 m^2). Atik et al. (2022) proposed a deep learning framework for adaptive change detection, using convolutional neural networks (CNN) to extract multi-temporal features, achieving 91.5% detection accuracy in complex construction environments. However, the model's reliance on a large amount of labelled data limits its applicability in data-scarce regions.

In summary, existing construction disturbance classification methods still face limitations in feature extraction, computational efficiency, and adaptability. To address these challenges, this study proposes an AI-driven detection model aimed at improving classification accuracy and dynamic monitoring capability for construction disturbance

areas while enabling adaptive optimisation of classification standards. The key innovation of this study lies in integrating the strengths of fractal network evolution algorithm (FNEA), GA, and CNN to construct a spectral-texture-shape multidimensional feature space and develop a temporal feature analysis framework, enhancing the recognition capability of change detection methods across different construction stages. The objective is to achieve precise monitoring and adaptive classification adjustments for disturbance areas in complex construction environments.

2 Development of a detection and classification model for construction disturbance areas based on remote sensing data

This section presents a construction disturbance classification model. Section 2.1 employs FNEA for image segmentation to identify construction areas and classify different disturbance types. Section 2.2 integrates temporal information to monitor the changes in construction areas and optimises the classification method to achieve high detection accuracy.

2.1 AI-driven FNEA feature recognition method for construction disturbance areas

In practical applications, remote sensing images may suffer from geometric distortion, noise interference, and spectral inconsistencies, which directly affected the reliability of feature extraction and classification accuracy (Peters et al., 2022). To address these issues, this study adopted the FNEA to construct a classification framework and incorporated GA-based optimisation and CNN-based parameter tuning to achieve high-precision identification of construction disturbance areas. During the preprocessing stage of remote sensing data, radiometric and geometric corrections were performed on the original images to ensure data accuracy and consistency. The radiometric correction is expressed as equation (1).

$$L_{corr} = \frac{\mathrm{DN} - \mathrm{DN}_{\min}}{\mathrm{DN}_{\max} - \mathrm{DN}_{\min}} \left(L_{\max} - L_{\min} \right) + L_{\min} \tag{1}$$

In equation (1), L_{corr} represents the corrected radiance value; $L_{\max}$ and $L_{\min}$ are the maximum and minimum radiance values; DN denotes the pixel value of the original image; $\mathrm{DN}_{\min}$ and $\mathrm{DN}_{\max}$ are the minimum and maximum digital numbers used for normalisation. The feature space of construction disturbance areas consists of spectral, texture, and shape features, which work together to significantly improve classification accuracy. The regional mean spectral value is obtained using equation (2).

$$S_A = \frac{1}{n} \sum_{i=1}^{n} P_i \tag{2}$$

In equation (2), S_A represents the spectral feature value; P_i denotes the spectral value of the i^{th} pixel; and n is the total number of pixels. This feature distinguishes construction areas (e.g., bare soil) from vegetation-covered areas. Texture features are computed using the GLCM, as illustrated in equation (3).

$$C_{GLCM} = \sum_{i=1}^{K}\sum_{j=1}^{K}(i-j)^2 \times P(i,\ j) \tag{3}$$

In equation (3), C_{GLCM} represents the texture contrast; $P(i, j)$ signifies the joint probability of grey levels i and j; K is the number of grey levels, typically set to 256. A higher contrast value indicates rougher surface textures (e.g., tire tracks from construction machinery). Shape features are characterised by calculating the compactness of the region, as depicted in equation (4).

$$C = \frac{4\pi A}{P^2} \tag{4}$$

In equation (4), C represents compactness; A is the size of the region; and P is the boundary of the region. The compactness C approaches 1 for circular regions; irregular construction disturbances typically yield lower C values. The FNEA is applied for image segmentation, which follows a top-down segmentation approach, as evident in Figure 1.

Figure 1 Schematic diagram of image segmentation (see online version for colours)

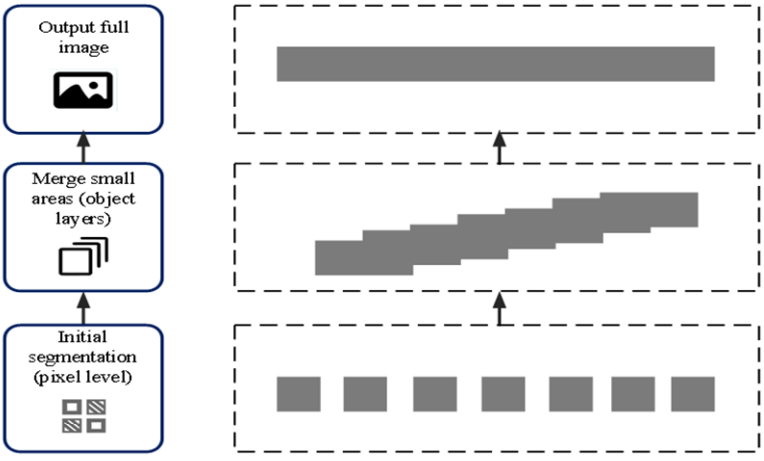

In Figure 1, the image is segmented using a top-down approach that merges pixels iteratively. The goal of image segmentation is to minimise the heterogeneity between pixels and objects, as expressed in equation (5).

$$H = \sum_{o \in O} d(p, o) \tag{5}$$

In equation (5), H represents the heterogeneity of segmented objects; O represents the set of segmented objects; p_i is the pixel; and $d(p,\ o)$ represents the distance measure considering spectral, texture, and shape differences. FNEA iteratively merges adjacent pixels to generate homogeneous objects, effectively avoiding the 'salt-and-pepper noise' problem in traditional segmentation methods (Shahid et al., 2022). The FNEA image segmentation method relies on multi-scale segmentation parameter settings, where the scale parameter determines the object size, and the consistency criterion balances spectral

and shape factors to enhance classification accuracy. The composition of image segmentation parameters is apparent in Figure 2.

Figure 2 Composition of image segmentation parameters (see online version for colours)

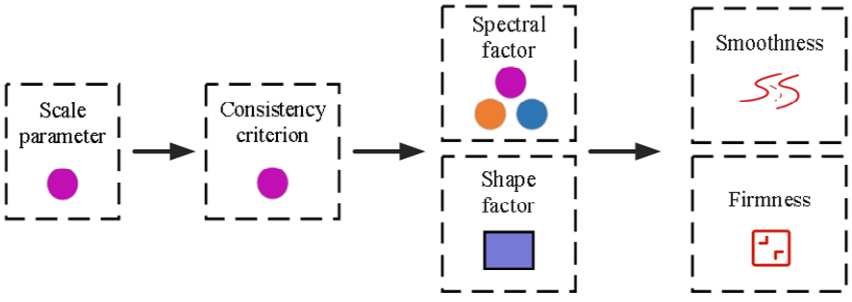

Figure 2 presents the parameter system of FNEA image segmentation. Proper parameter settings optimise segmentation results, reduce noise, and improve classification accuracy. Feature extraction is performed through the weighted fusion of multiple features, as shown in equation (6).

$$\mathbf{F} = \sum_{k=1}^{m} w_k \times f_k \tag{6}$$

In equation (6), **F** represents the comprehensive feature value; w_k denotes the weight of the k^{th} feature, which is optimised through the evolutionary algorithm; and f_i represents the normalised feature value. The FNEA classification rule is constructed based on the similarity between objects and categories, as shown in equation (7).

$$S\left(x, C_j\right) = -x\left(x-\mu_j\right)^{\top} \sum\nolimits_j^{-1} \left(x-\mu_j\right) \tag{7}$$

In equation (7), $S(x, C_j)$ represents the similarity between objects x and categories C_j, which is calculated based on the Mahalanobis distance. This FNEA classification rule dynamically adjusts feature weights to adapt to different construction environments. FNEA optimises classifier parameters using GA, as expressed in equation (8).

$$\boldsymbol{\theta}^{(t+1)} = \boldsymbol{\theta}^{(t)} + \eta \Delta \boldsymbol{\theta} \tag{8}$$

In equation (8), $\boldsymbol{\theta}^{(t+1)}$ and $\boldsymbol{\theta}^{(t)}$ represent the new and old classifier parameters, respectively; η is the learning rate; and $\Delta\boldsymbol{\theta}$ denotes the parameter change, which is generated through crossover and mutation operations. The classification threshold is adaptively adjusted using deep learning, as expressed in equation (9).

$$\tau' = \tau + \alpha \Delta \tau \tag{9}$$

In equation (9), τ' represents the adjusted classification threshold; τ is the original classification threshold; α denotes the adjustment coefficient; and $\Delta\tau$ represents the threshold variation, which is calculated through backpropagation of the CNN based on validation set errors. The overall workflow for construction-disturbance detection and classification is shown in Figure 3.

Figure 3 Workflow for construction-disturbance area recognition based on FNEA, GA, and CNN (see online version for colours)

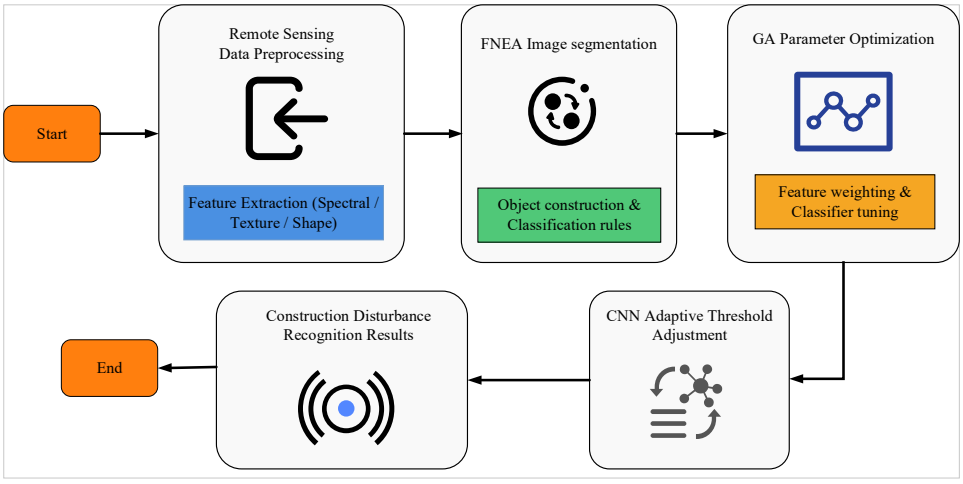

As shown in Figure 3, the process starts with remote-sensing data preprocessing. After extracting spectral, texture, and shape features, FNEA performs image segmentation and sets the classification rules. GA then tunes the feature weights and classifier parameters. Finally, CNN adaptively adjusts the classification threshold to produce the recognition results for construction-disturbance areas.

2.2 Construction of a dynamic monitoring and classification model for construction disturbance based on multi-feature change detection

The previous section introduced the extraction and classification of static construction disturbance areas. This section further addresses the challenge of real-time monitoring for dynamic construction disturbances. Traditional methods typically rely on single-phase data or individual features for analysis, making it difficult to comprehensively capture the dynamic changes in construction disturbances. This study integrated multi-temporal change detection methods to develop an AI-driven dynamic monitoring model, enhancing real-time detection capabilities. The overall process is illustrated in Figure 4.

As shown in Figure 4, the model determines construction disturbance areas based on brightness difference, texture variation, and shape features. AI is utilised to optimise classification standards, improving both real-time performance and accuracy in dynamic monitoring. The specific feature construction process is detailed as follows. First, to obtain remote sensing images at different time points, a multi-temporal dataset is established, as expressed in equation (10).

$$X_t = \{S_t, T_t, G_t\}. \tag{10}$$

In equation (10), X_t represents the multi-temporal feature vector, which denotes the feature set of the construction disturbance area at time t; S_t corresponds to spectral features; T_t represents texture features; G_t denotes shape features, describing geometric characteristics such as area, perimeter, compactness, and roundness at time t, which help distinguish construction areas from natural changes. By integrating spectral, texture, and

shape features, this formula constructs a multi-temporal feature set for construction disturbance areas, enabling accurate identification and classification of disturbance changes. The brightness difference method is then applied to detect disturbance changes, as defined in equation (11).

$$\Delta B = B_t - B_{t-1} \tag{11}$$

In equation (11), ΔB represents the brightness difference; B_t is the brightness at time t; B_{t-1} represents the brightness at time $t-1$. To describe texture feature variations in the images, the GLCM is used to extract greyscale directional information, as illustrated in Figure 5.

Figure 4 Workflow of the dynamic monitoring and classification model for construction disturbance (see online version for colours)

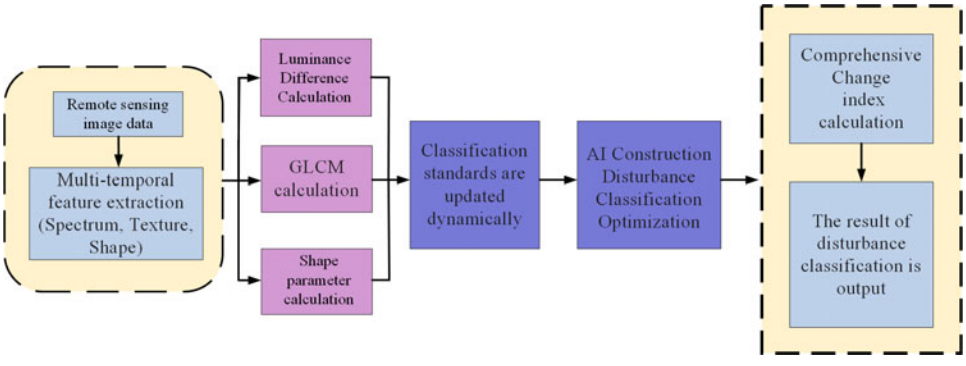

Figure 5 Grey-level co-occurrence matrix (see online version for colours)

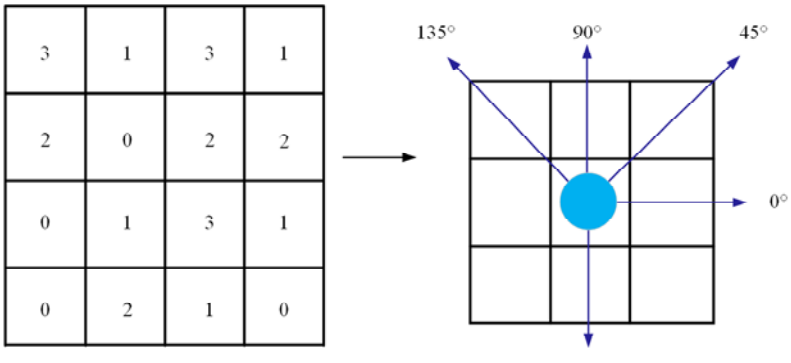

Figure 5 demonstrated the GLCM calculation process at different angles (0°, 45°, 90°, 135°). Texture feature variations are analysed by constructing a co-occurrence matrix, as given in equation (12).

$$\Delta T = T_t - T_{t-1} \tag{12}$$

In equation (12), ΔT represents the texture variation value, quantifying the degree of texture change between two time points t and $t-1$. A larger value indicates a greater impact of construction disturbance on surface texture. T_t and T_{t-1} represent the texture

feature at times t and $t - 1$, describing the greyscale relationships among image pixels. Shape variation detection is formulated in equation (13).

$$\Delta C = C_t - C_{t-1} \tag{13}$$

In equation (13), ΔC represents the updated classification result. Construction disturbance often results in $\Delta C < 0$, as newly added disturbed areas tend to have more irregular shapes. C_t and C_{t-1} are the shape feature values at the new and previous time points. The integrated change index is defined in equation (14).

$$I = \beta_1 \Delta B + \beta_2 \Delta T + \beta_{33} \Delta C \tag{14}$$

In equation (14), I represents the integrated change index. If this value exceeds a threshold, it is classified as a significant disturbance change. β_1, β_2 and β_3 correspond to the weights of brightness, texture, and shape variations, respectively. AI-based classification is then applied to dynamically categorise disturbed areas and optimise classification standards, as described in equation (15).

$$P(y = 1|X) = \frac{1}{1 + e^{-(\mathbf{w}^\top x + b)}} \tag{15}$$

In equation (15), $P(y = 1|X)$ represents the probability that the input features X represents the input feature vector; $\mathbf{w}$ is the weight vector; b is the bias term; e is the base of the natural logarithm, approximately 2.718. To enhance accuracy in dynamic monitoring, the approach is optimised by minimising a decrease in the cross function with regularisation, as given in equation (16).

$$\mathcal{L} = -\frac{1}{N} \sum_{i=1}^{N} \left[y_i \log \hat{y}_i + (1 - y_i) \log (1 - \hat{y}_i) \right] + \lambda \|\mathbf{w}\|^2 \tag{16}$$

In equation (16), L denotes the loss function; N represents the number of samples; y_i is the true class label; $\hat{y}_i$ is the predicted value computed by the classification model; λ is the regularisation coefficient, which controls model complexity to prevent overfitting; $\|\mathbf{w}\|$ is the norm of the weight vector, constraining model weights to avoid excessive values, thereby improving generalisation ability. To further enhance adaptability, AI dynamically adjusts classification standards in real-time, as formulated in equation (17).

$$\Gamma' = \Gamma + \delta \Delta \Gamma \tag{17}$$

In equation (17), Γ' represents the updated classification standard; Γ is the original classification standard; δ is the update coefficient; $\Delta\Gamma$ denotes the standard variation.

3 Verification of the construction disturbance area detection and classification model based on remote sensing data

To validate the effectiveness of the proposed static classification model (Section 3.1) and dynamic monitoring model (Section 3.2), this section conducts a comprehensive evaluation through experimental design and comparative analysis in terms of classification accuracy, robustness, and real-time performance.

3.1 Validation of AI-driven FNEA construction disturbance area feature recognition method

This study used multi-source remote sensing data, including optical and radar imagery:

1 Sentinel-2 data provided by the European Space Agency (ESA), with 10 m spatial resolution and a 5-day revisit, collected from January 2020 to June 2024

2 Landsat-8 data released by the US Geological Survey (USGS), with 30 m spatial resolution and a 16-day revisit, covering the same period as Sentinel-2

3 synthetic aperture radar (SAR) data from the Sentinel-1 mission, with 10 m resolution, available under cloudy conditions.

These datasets cover typical construction-disturbance scenarios such as road building, mining, and urban expansion, with 2,400 image samples in total. Ground truth was obtained by:

1 manual interpretation of unmanned aerial vehicle (UAV) images at 0.2 m accuracy to delineate disturbance areas

2 consulting local government planning documents and construction records to confirm disturbance types and stages

3 field surveys in representative regions to validate the interpretations.

The final annotated set contains 18,000 samples of disturbed and non-disturbed areas for model training and validation. The FNEA parameters are set as follows: initial segmentation scale = 50, heterogeneity weight (spectrum: texture: shape) = 0.6:0.3:0.1. The dynamic model parameters were: CCI threshold = 0.7, learning rate $\eta = 0.01$, and regularisation coefficient $\lambda = 0.1$.

To assess the effectiveness of the proposed method (FNEA+GA+CNN), representative baselines were selected for comparison:

1 support vector machine (SVM), a classical supervised classifier based on the maximum-margin principle, widely used in remote-sensing scene classification and effective for small-to-medium samples and high-dimensional features

2 random forest (RF), an ensemble of decision trees via bagging, known for robustness and low sensitivity to noise, often adopted for stable classification of multi-source features

3 U-Net convolutional neural network (U-Net), an encoder-decoder semantic segmentation network suited to end-to-end pixel-level classification and a strong baseline for land-cover segmentation.

Additionally, an ablation experiment is conducted to further analyse the effectiveness of the proposed method by comparing the classification performance of FNEA combined with different optimisation strategies (GA, CNN). The evaluation metrics include OA, kappa and F1-score, as shown in Table 1.

Table 1 Comparison of classification accuracy of different methods (mean ± SD, 95% CI in parentheses)

Method	*OA (%)*	*Kappa*	*F1 (construction class)*
SVM	82.3 ± 1.5 (95% CI: 81.4–83.2)	0.74 ± 0.02 (95% CI: 0.73–0.75)	0.68 ± 0.03 (95% CI: 0.67–0.69)
RF	85.6 ± 1.2 (95% CI: 84.9–86.3)	0.79 ± 0.02 (95% CI: 0.78–0.80)	0.73 ± 0.02 (95% CI: 0.72–0.74)
U-Net	88.1 ± 0.9 (95% CI: 87.6–88.6)	0.82 ± 0.01 (95% CI: 0.81–0.83)	0.76 ± 0.02 (95% CI: 0.75–0.77)
FNEA	91.4 ± 0.7 (95% CI: 91.0–91.8)	0.87 ± 0.01 (95% CI: 0.86–0.88)	0.82 ± 0.01 (95% CI: 0.81–0.83)
FNEA + GA	92.8 ± 0.6 (95% CI: 92.4–93.2)	0.89 ± 0.01 (95% CI: 0.88–0.90)	0.84 ± 0.01 (95% CI: 0.83–0.85)
FNEA + CNN	93.5 ± 0.5 (95% CI: 93.2–93.8)	0.90 ± 0.01 (95% CI: 0.89–0.91)	0.85 ± 0.01 (95% CI: 0.84–0.86)
FNEA + GA + CNN (proposed)	95.2 ± 0.4 (95% CI: 95.0–95.4)	0.93 ± 0.01 (95% CI: 0.92–0.94)	0.88 ± 0.01 (95% CI: 0.87–0.89)

Note: Results are reported as mean ± standard deviation (SD) with 95% confidence intervals (CI), computed from n = 10 independent runs.

Table 1 showed that the proposed method outperformed other comparison methods in terms of OA, kappa and F1-score, achieving an OA of 95.2% ± 0.4% (95% CI [95.0, 95.4]), a kappa coefficient of 0.93 ± 0.01 (95% CI [0.92, 0.94]), and an F1-score of 0.88 ± 0.01 (95% CI [0.87, 0.89]). Compared to using only FNEA (OA = 91.4% ± 0.7%), incorporating GA optimisation (FNEA + GA) improved classification accuracy to 92.8% ± 0.6% (95% CI [92.4, 93.2]), while further integration of CNN feature fusion (FNEA + CNN) enhanced classification accuracy to 93.5% ± 0.5% (95% CI [93.2, 93.8]). These results indicated that the proposed multi-feature fusion and evolutionary optimisation mechanism effectively adapted to complex construction scenarios. The classification results based on remote sensing images were quantitatively analysed using manual visual interpretation data to extract features of disturbance areas in construction scenes for 2021 and 2023. Producer accuracy, user accuracy, overall accuracy and kappa coefficient were adopted as evaluation metrics to assess the stability of the proposed classification method and its effectiveness in extracting disturbance areas, as shown in Figure 6.

In Figure 6(a), the proposed method achieved user accuracy of 80.2% ± 1.4% in 2021 and 79.8% ± 1.6% in 2023, staying close to 80%. In Figure 6(b), the producer accuracy for disturbance areas in both years is around 83%, indicating that the method effectively extracts disturbance area information. Figure 5(c) shows that the overall accuracy reached 99.63% ± 0.21% (2021) and 99.02% ± 0.24% (2023), demonstrating reliable classification results. The kappa coefficient is 0.8247 ± 0.012 in 2021 and 0.8137 ± 0.015 in 2023, close to 1, indicating high agreement between classification results and actual conditions with minimal misclassification. These results confirm that the proposed method accurately identifies disturbance areas and remains stable over different time periods. Next, the dynamic monitoring performance of the proposed multi-feature fusion method for disturbance areas is verified.

Figure 6 Stability and accuracy verification of the proposed classification method, (a) user accuracy comparison (b) producer accuracy comparison (c) comparison of total precision and kappa coefficient (see online version for colours)

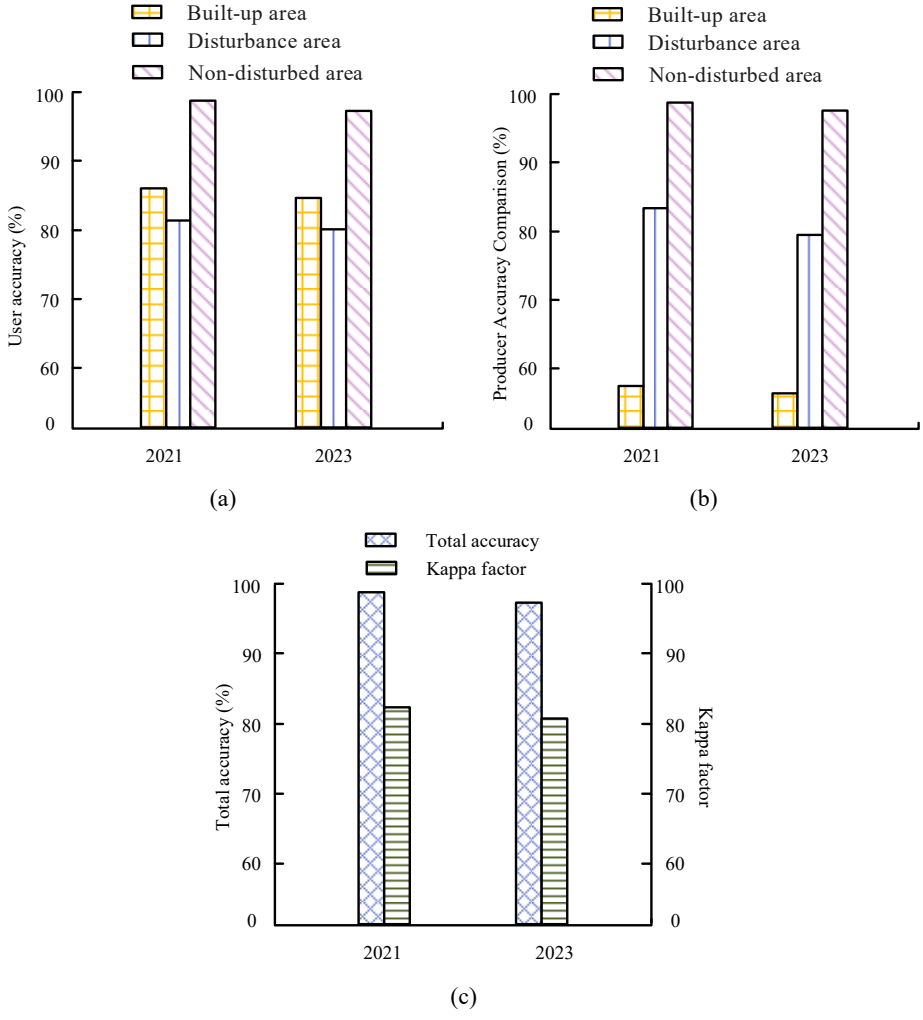

Note: Results are reported as mean ± SD, based on n = 10 independent runs. The same convention applies below.

3.2 *Verification of the construction disturbance dynamic monitoring and classification model based on multi-feature change detection*

The results from the previous section indicate that the proposed static feature recognition classification method achieves high accuracy and stability. Next, the dynamic monitoring performance of the proposed multi-feature fusion method for disturbance areas is verified. The proposed multi-feature change detection method is compared in accuracy with advanced deep learning and feature fusion methods, transformer and MS-FFN, as shown in Figure 7.

Figure 7 Comparison of change detection accuracy for three methods (a) producer accuracy comparison (b) producer accuracy comparison (see online version for colours)

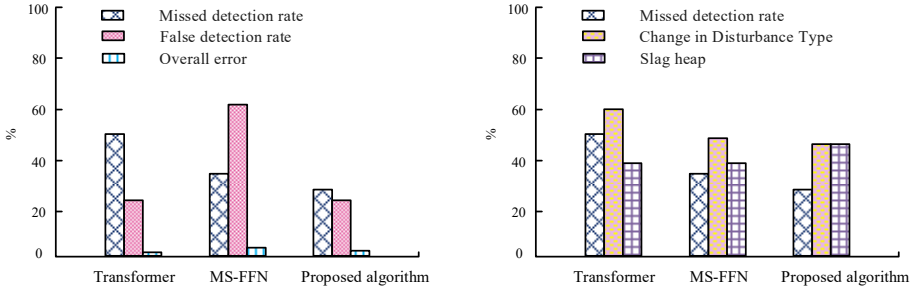

Figure 7(a) presented the change detection performance. The proposed method achieved the lowest false positive rate and false negative rate, at 31.35% ± 1.2% and 23.18% ± 1.0%, respectively. Meanwhile, the overall error rate of the proposed method was 1.35% ± 0.3%, which is 0.73% and 0.36% lower than those of transformer and MS-FFN, respectively. Figure 7(b) showed that transformer has the highest false positive rate (52.67% ± 1.5%) due to misclassification caused by disturbance type changes (60%) and soil accumulation (40%). MS-FFN had a lower false positive rate (36.17% ± 1.3%), with misclassification proportions of 55% and 45% for disturbance type changes and soil accumulation, respectively. The proposed method achieved the lowest false positive rate (31.64% ± 1.1%), with an equal misclassification proportion of 50% for disturbance type changes and soil accumulation. Change vector analysis (CVA) is used as a comparison method. CVA is a classical change detection method, making it suitable for comparing the performance differences between multi-feature fusion and single-feature methods. The error rates for newly added disturbance areas, new buildings, and newly added non-disturbance areas serve as evaluation metrics, as shown in Figure 8.

Figure 8(a) showed that the proposed method had an error rate of 2.6% ± 0.4%, which is 5.2% lower than that of CVA. The newly added area calculated by the proposed method was 662.6 ± 12.4 hm^2, closest to the actual value of 649.2 hm^2. Figure 8(b) indicated that the proposed method achieves the lowest misclassification rates for newly added buildings and non-disturbance areas, at 21.76 ± 2.1 hm^2 and 27.13 ± 2.4 hm^2, respectively, demonstrating stronger classification differentiation capability. These results confirmed that the proposed method, by utilising multiple features for classification, achieved higher accuracy and reliability in disturbance area monitoring. To verify the effectiveness of the proposed algorithm (FNEA + GA + CNN) in optimisation problems, it was compared with quantum genetic algorithm (QGA), particle swarm optimisation (PSO) and transformer (a deep learning model). These algorithms represent three different approaches: intelligent optimisation, heuristic search, and complex feature extraction. The fitness values of each method on different datasets are compared, as shown in Figure 9.

Figure 8 Comparison of dynamic detection errors for two feature fusion methods, (a) comparison of errors in the area of additional disturbed areas detected by different methods (b) misclassification comparison of new buildings and non-disturbed areas (see online version for colours)

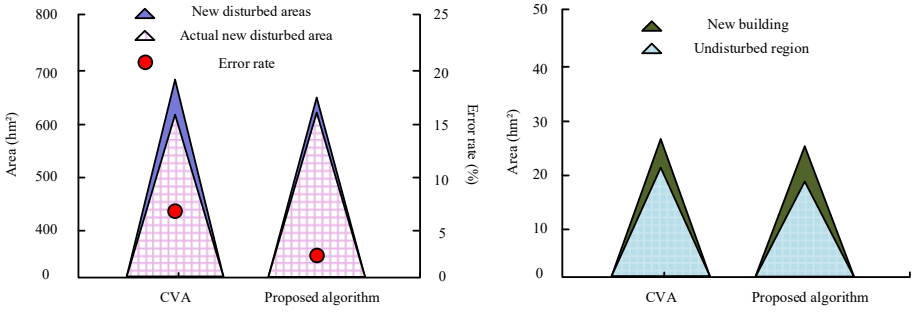

Figure 9 Fitness function curves for different methods, (a) road construction (b) mining (c) urban expansion (d) comprehensive construction (see online version for colours)

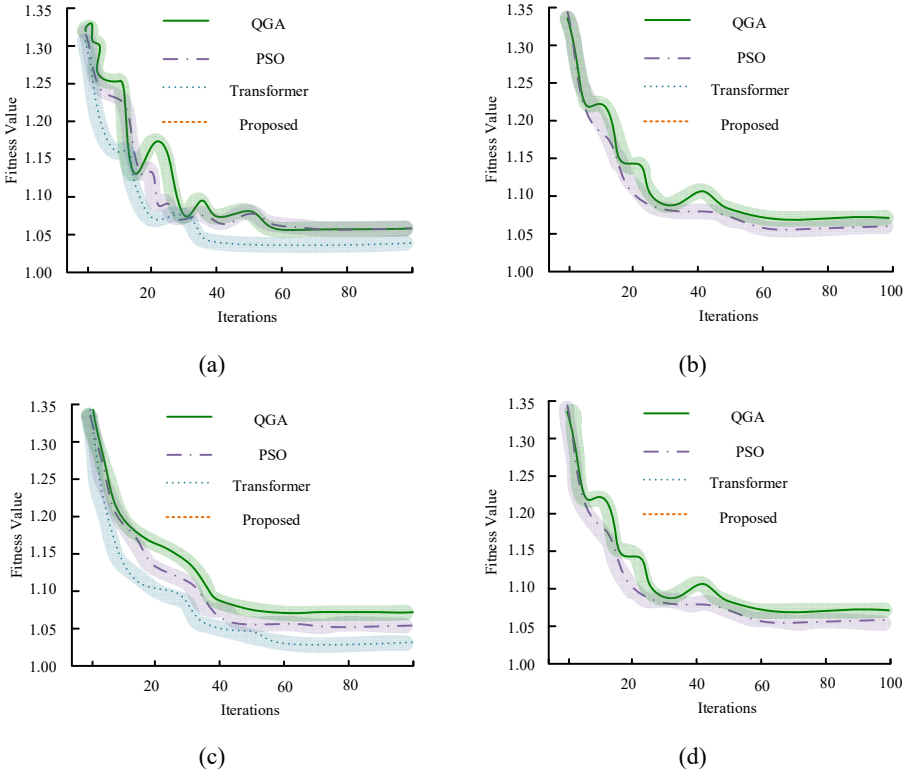

Note: Curves show the mean, and the shaded area denotes ±SD, computed over n = 10 independent runs.

Figure 9(a) showed that the proposed algorithm reached the optimal solution within 30 iterations, while other methods achieved the optimal solution only after 100 iterations. In Figure 9(b), the proposed method converged to a fitness value of 1.06 ± 0.03 within 20 iterations and stabilised at 1.01 ± 0.02 after 40 iterations. Figure 9(c) demonstrated that the proposed method rapidly converged within the first 20 iterations and ultimately stabilised at 1.00 ± 0.02. Figure 9(d) showed that the proposed method reached a fitness value of 1.05 ± 0.02 within 20 iterations and finally stabilises at 1.01 ± 0.01. These results indicated that the proposed method surpassed others in both convergence speed and accuracy. Next, the receiver operating characteristic (ROC) curves of the lightweight gradient boosting machine (LightGBM) and extreme gradient boosting (XGBoost) are compared on training and testing datasets, as shown in Figure 10.

Figure 10 ROC curves of different algorithms, (a) training set (b) test set (see online version for colours)

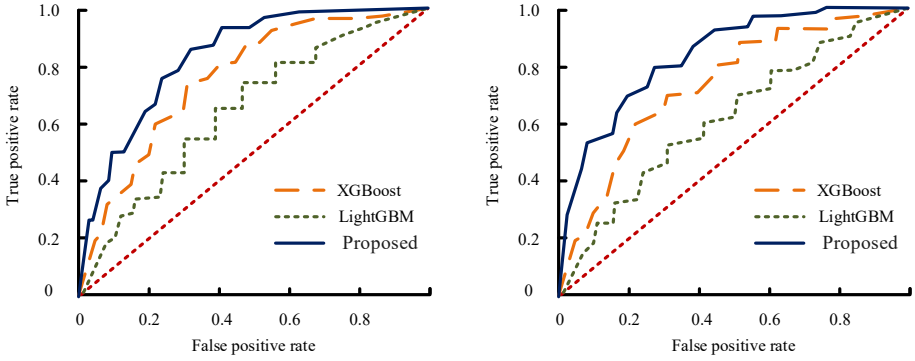

Note: Curves present the mean; AUC is given as mean ± SD (95% CI), calculated over n = 10 independent runs.

Figure 10 showed that the proposed method's ROC curve was closer to the top-left corner, indicating a higher AUC and overall classification performance. In Figure 10(a), the proposed method achieved an AUC of 0.95 ± 0.02 (95% CI [0.93, 0.97]), surpassing XGBoost (0.85 ± 0.03，95% CI [0.82, 0.88]) and LightGBM (0.88 ± 0.02, 95% CI [0.86, 0.90]). In Figure 10(b), the proposed method maintained a significant advantage in AUC, with the smallest degradation 5.3% ± 0.6% (95% CI [4.8%, 5.9%]). These results confirmed that the proposed method outperformed the comparison methods in classification accuracy and generalisation ability, with its smaller degradation proving its superior adaptability to unknown data.

4 Conclusions

Accurately identifying and dynamically monitoring construction disturbance areas can help the government in urban planning, environmental protection, and land management (Karuppiah et al., 2022). However, existing methods for detecting construction disturbances struggle to ensure high classification accuracy and precise detection of

multi-temporal changes. Based on this, this study presented a method to recognise construction disturbances via FNEA segmentation. The method employed FNEA for image segmentation, optimised classification parameters through GA, and incorporated CNN for feature learning, which enhanced classification accuracy and the stability of dynamic monitoring.

The results indicated that the proposed method demonstrated significant advantages in construction disturbance detection. The method achieved an OA of 95.2% ± 0.4% (95% CI [95.0–95.4]), a kappa value of 0.93 ± 0.01 (95% CI [0.92–0.94]), and an F1 grade of 0.88 ± 0.01 (95% CI [0.87, 0.89]), which is a notable improvement compared to the U-Net method proposed by Sun and Wu (2022b) (F1 = 0.84). Particularly in dynamic monitoring tasks for construction disturbances, the classification accuracy reached 99.63% ± 0.21% in 2021 and 99.02% ± 0.24% in 2023, while the false detection rate and missed detection rate dropped to 31.35% ± 1.2% and 23.18% ± 1.0%, respectively. As compared to the transformer and MS-FFN takes on suggested by Sun and Wu (2022a) and Xiao et al. (2023) the strategy put forward is more robust. In contrast to the U-Net method introduced by Singh and Sharma (2021), the method in this study demonstrates greater adaptability. Testing on different datasets showed that the proposed method converged within 20–30 iterations, which was significantly faster than the 100 iterations required by QGA and PSO, improving computational efficiency by approximately 70%. Meanwhile, the proposed method achieved an AUC value of 0.95 ± 0.02 (95% CI [0.93, 0.97]), whereas XGBoost and LightGBM obtained only 0.85 ± 0.03 (95% CI [0.82, 0.88]) and 0.88 ± 0.02 (95% CI [0.86, 0.90]), respectively, proving its strong generalisation ability across different datasets.

In conclusion, the proposed construction disturbance detection method not only improves classification accuracy but also enhances dynamic monitoring stability and optimises computational efficiency, providing an efficient and intelligent solution for remote sensing monitoring in complex construction environments. However, several limitations remain: the study area was limited and cross-regional generalisation has not yet been verified; high-precision detection relies on large labelled data, which is costly; and higher-resolution or multi-source data were not fully used. Future work may explore cross-region transfer and adaptation, apply semi-supervised or interactive labelling to reduce data cost, and integrate heterogeneous multi-source data with distributed computing to further improve adaptability and practicality.

Declarations

All authors declare that they have no conflicts of interest.

References

Ahmad, M.N., Shao, Z. and Javed, A. (2023a) ‘Modelling land use/land cover (LULC) change dynamics, future prospects, and its environmental impacts based on geospatial data models and remote sensing data’, *Environmental Science and Pollution Research*, Vol. 30, No. 12, pp.32985–33001.

Ahmad, M.N., Shao, Z., Javed, A., Islam, F., Ahmad, H.H. and Aslam, R.W. (2023b) ‘The cellular automata approach in dynamic modelling of land use change detection and future simulations based on remote sensing data in Lahore Pakistan’, *Photogrammetric Engineering & Remote Sensing*, Vol. 89, No. 1, pp.47–55.

Atik, S.O., Atik, M.E. and Ipbuker, C. (2022) 'Comparative research on different backbone architectures of DeepLabV3+ for building segmentation', *Journal of Applied Remote Sensing*, Vol. 16, No. 2, p.024510.

Casagli, N., Intrieri, E., Tofani, V., Gigli, G. and Raspini, F. (2023) 'Landslide detection, monitoring and prediction with remote-sensing techniques', *Nature Reviews Earth & Environment*, Vol. 4, No. 1, pp.51–64.

Darem, A.A., Alhashmi, A.A., Almadani, A.M., Alanazi, A.K. and Sutantra, G.A. (2023) 'Development of a map for land use and land cover classification of the northern border region using remote sensing and GIS', *The Egyptian Journal of Remote Sensing and Space Science*, Vol. 26, No. 2, pp.341–350.

Guo, B., Lu, M., Fan, Y., Nguyen, K. and Dur, F. (2023) 'A novel remote sensing monitoring index of salinization based on three-dimensional feature space model and its application in the Yellow River Delta of China', *Geomatics, Natural Hazards and Risk*, Vol. 14, No. 1, pp.95–116.

Karuppiah, S.P., Sheeba, A., Padmakala, S. and Subasin, C.A. (2022) 'An efficient galactic swarm optimization based fractal neural network model with DWT for malignant melanoma prediction', *Neural Processing Letters*, Vol. 54, No. 6, pp.5043–5062.

Li, J., Huang, X., Tu, L., Zhang, T. and Wang, L. (2022) 'A review of building detection from very high resolution optical remote sensing images', *GIScience & Remote Sensing*, Vol. 59, No. 1, pp.1199–1225.

Liu, Z., Xu, J., Liu, M., Yin, Z., Liu, X., Yin, L. and Zheng, W. (2023) 'Remote sensing and geostatistics in urban water-resource monitoring: a review', *Marine and Freshwater Research*, Vol. 74, No. 10, pp.747–765.

Lv, N., Zhang, Z., Li, C., Deng, J., Su, T., Chen, C. and Zhou, Y. (2023) 'A hybrid-attention semantic segmentation network for remote sensing interpretation in land-use surveillance', *International Journal of Machine Learning and Cybernetics*, Vol. 14, No. 2, pp.395–406.

Padhy, R., Dash, S.K., Khandual, A. and Mishra, J. (2023) 'Image classification in artificial neural network using fractal dimension', *International Journal of Information Technology*, Vol. 15, No. 6, pp.3003–3013.

Peters, R., Dukai, B., Vitalis, S., van Liempt, J. and Stoter, J. (2022) 'Automated 3D reconstruction of LoD2 and LoD1 models for all 10 million buildings of the Netherlands', *Photogrammetric Engineering & Remote Sensing*, Vol. 88, No. 3, pp.165–170.

Shahid, M., Ashraf, Z., Shamim, M. and Ansari, M.S. (2022) 'Solving constrained portfolio optimization model using stochastic fractal search approach', *International Journal of Intelligent Computing and Cybernetics*, Vol. 16, No. 2, pp.223–249.

Shen, H., Jiang, M., Li, J., Zhou, C., Yuan, Q. and Zhang, L. (2022) 'Coupling model- and data-driven methods for remote sensing image restoration and fusion: improving physical interpretability', *IEEE Geoscience and Remote Sensing Magazine*, Vol. 10, No. 2, pp.231–249.

Singh, S.P. and Sharma, S.C. (2021) 'A PSO-based improved clustering algorithm for lifetime maximisation in wireless sensor networks', *International Journal of Information and Communication Technology*, Vol. 18, No. 2, pp.224–241.

Sun, Q. and Wu, Q. (2022a) 'Feature space fusion classification of remote sensing image based on ant colony optimisation algorithm', *International Journal of Information and Communication Technology*, Vol. 20, No. 2, pp.164–176.

Sun, Q. and Wu, Q. (2022b) 'Target similarity matching algorithm of big data in remote sensing image based on Henon mapping', *International Journal of Information and Communication Technology*, Vol. 20, No. 1, pp.51–64.

Wang, L., Wang, J., Liu, Z., Zhu, J. and Qin, F. (2022) 'Evaluation of a deep-learning model for multispectral remote sensing of land use and crop classification', *The Crop Journal*, Vol. 10, No. 5, pp.1435–1451.

Xiao, S., Liu, J. and Xu, P. (2023) 'Real-time recommendation method of online education resources based on improved decision tree algorithm', *International Journal of Information and Communication Technology*, Vol. 23, No. 4, pp.388–400.

Xu, Y., Huang, H., Li, Y., Zhou, J., Lu, X. and Wang, Y. (2022) 'A three-stage online anomaly identification model for monitoring data in dams', *Structural Health Monitoring*, Vol. 21, No. 3, pp.1183–1206.

Yang, S., Zhao, C., Yang, Y., Ren, J. and Ling, S. (2023) 'The fractal network structure of silk fibroin molecules and its effect on spinning of silkworm silk', *ACS Nano*, Vol. 17, No. 8, pp.7662–7673.

Zeng, Y., Guo, Y. and Li, J. (2022) 'Recognition and extraction of high-resolution satellite remote sensing image buildings based on deep learning', *Neural Computing and Applications*, Vol. 34, No. 4, pp.2691–2706.